Article:
Jia, C., Zhu, X., Su, W. et al. (Accepted: 2026) Protracted ocean oxygenation in the early Mesoproterozoic. Communications Earth & Environment. ISSN: 2662-4435 (In Press)

Protracted ocean oxygenation in the early Mesoproterozoic

Chaoyuan Jia[1,2], Xiyan Zhu[1,2 *], Wenbo Su[3], Simon W. Poulton[4], Taiping Zhao[5], Andrey Bekker[6,7 *]

[1] *State Key Laboratory of Lithospheric and Environmental Coevolution, Institute of Geology and Geophysics, Chinese Academy of Sciences, Beijing 100029, China*

[2] *School of Earth and Planetary Sciences, University of Chinese Academy of Sciences, Beijing 101408, China*

[3] *School of Earth Sciences and Resources, China University of Geosciences, Beijing 100083, China*

[4] *School of Earth, Environment and Sustainability, University of Leeds, Leeds LS2 9JT, UK*

[5] *State Key Laboratory of Deep Earth Processes and Resources, Guangzhou Institute of Geochemistry, Chinese Academy of Sciences, Guangzhou 510640, China*

[6] *Department of Earth and Planetary Sciences, University of California, Riverside, CA 92521, USA*

[7] *Department of Geology, University of Johannesburg, P.O. Box 524, Auckland Park, Johannesburg 2006, South Africa*

* Corresponding authors. E-mail and ORCID link:

zhuxiyan@mail.iggcas.ac.cn (Xiyan Zhu); https://orcid.org/0000-0003-0396-6348

andrey.bekker@ucr.edu (Andrey Bekker); https://orcid.org/0000-0002-1154-0585

Keywords: Oxygenation; Seawater redox conditions; Mid-Proterozoic; Ectasian Period; Baishugou Formation; North China Craton

Abstract

Emerging evidence suggests that, against a backdrop of generally low atmospheric oxygen levels, the mid-Proterozoic (ca. 1.8–0.8 Ga) ocean may have experienced transient oxygenation events, potentially peaking at ca. 1.4 Ga. However, whether these events were short-lived or represent enhanced longer-term oxygenation remains uncertain. Here, we present molybdenum isotope ($\delta^{98/95}$Mo), iron speciation, redox-sensitive trace element and nutrient data for the ca. 1.33 Ga Baishugou Formation on the southern margin of the North China Craton. Our data document a stable

oxygen-minimum zone featuring an euxinic to ferruginous core surrounded by dysoxic to oxic waters. In the euxinic interval, $\delta^{98/95}$Mo values are notably high (up to +1.62‰), indicating expanded ocean oxygenation. Combined with existing geochemical records, we suggest that the early Ectasian (1.4–1.3 Ga) was characterized by a sustained interval of relatively high oxygen availability in the oceans rather than episodic pulses, likely creating conditions conducive to early eukaryotic diversification.

Introduction

The oxygenation of Earth's surface environment is thought to have occurred across three major periods: the Great Oxidation Episode (GOE), the Neoproterozoic Oxygenation Event (NOE) and the early Paleozoic Oxygenation Event (POE)[1–4]. The mid-Proterozoic (ca. 1.8–0.8 Ga) interval, bracketed between the GOE and NOE, is characterized by the absence of widespread glaciations and a generally invariant inorganic carbon isotope record ($\delta^{13}C_{carb}$ typically at 0 ± 2‰[5]), although distinct, small-amplitude carbon isotope excursions have recently been reported[6–8]. Atmospheric oxygen levels during this interval are highly debated, with estimates ranging from <1% of the present atmospheric level (PAL)[9,10] to ~4–10% PAL[11–13]. Emerging evidence from marine redox proxies has, however, challenged the paradigm of highly stable Earth system conditions, suggesting episodic oxygenation pulses during the mid-Proterozoic, at least in the marine realm[6–8,14]. These include intervals of enhanced oxygenation at ca. 1.59–1.56, 1.46–1.45, 1.44–1.43, 1.40–1.35 and 1.1–1.0 Ga[7,8,11,15–22]. These events are generally interpreted as transient pulses rather than sustained increase in atmospheric pO_2[7,22,23], although at least during the ca. 1.59–1.56 Ga event, successive pulses may have progressively increased oxygenation levels[7].

The North China Craton (NCC) has provided critical insight into this debate. For the Ectasian period (1.4–1.2 Ga) in particular, the ca. 1.40–1.35 Ga Xiamaling Formation on the northern margin of the NCC records elevated contents of redox-sensitive trace elements (RSTEs; e.g., Mo and U), and high I/(Ca+Mg) and $\delta^{98/95}$Mo values[18,20,24–26], suggesting that atmospheric oxygen levels may have exceeded 4% PAL[11,18,25]. The ca. 1.42–1.36 Ga Velkerri Formation in the McArthur Basin of the North Australian Craton[14], which is suggested to have been adjacent to the NCC in the Ectasian Period[27–29],

is also thought to record contemporaneous oxygenation[29,30]. However, due to an unconformity, ca. 300 million years of the sedimentary record is missing between the Xiamaling Formation and overlying Qingbaikou Group[31–33]. Thus, the subsequent evolution of oceanic redox conditions after the deposition of the Xiamaling Formation is unconstrained.

The southern margin of the NCC does, however, preserve an important sedimentary record through this interval. Here, we present Mo isotope data alongside local redox indicators (Fe speciation, RSTEs) for black shales of the ca. 1.33 Ga Baishugou Formation[34], which allow us to evaluate whether higher oxygenation levels were prevalent after deposition of the Xiamaling Formation in the early Ectasian, or whether the Earth system regressed to lower oxygenation levels. The sedimentary record during this period contains abundant organic-walled microfossils, some of which are of eukaryotic affinity[35]. Accordingly, we also discuss the implications of redox reconstruction in the context of environmental conditions that may have supported early eukaryotic diversification.

Results and Discussion

Geological background

The ~80–100 m-thick Baishugou Formation in the Xiong'er Basin of the southern NCC was deposited in a foreland basin developed along the northern margin of the NCC[34,36–38], with black shales as the primary lithology, interbedded with thin tuff beds. The silica-rich black shales exhibit an upsection increase in total organic carbon (C_{org}) within a succession that evolves from inner-shelf mudstones toward distal settings. While the broader sequence evolves toward coarser-grained distal turbidites, the black shales studied here were deposited exclusively in a low-energy, outer-shelf setting below storm wave-base (see Supplementary Information). LA-ICP-MS U-Pb zircon analyses of tuff beds in the middle of the black shale interval gave ages of 1330 ± 10 Ma and 1332 ± 10 Ma[34], suggesting that the Baishugou Formation is younger than the Xiamaling and Velkerri formations[14,31,39–41] (see Supplementary Information). Using tuff-bearing beds as marker beds, a relatively complete sequence was assembled by combining three distinct sections located in Yutang, Donggou'nao and Baishugou villages, from the base to the top of the Baishugou Formation. These sections are located only ~1–6 km apart (Supplementary Figure 1), in the same sedimentary facies

belt, thus enabling a detailed reconstruction of the basin-margin redox architecture. As such, the observed geochemical variations are interpreted to reflect migration of redox-defined facies, relative to the depositional site, driven by sea-level variations. The succession records a transgression from the Yutang section to the top of the Donggou'nao section, interpreted as a Transgressive Systems Tract (TST). This is bounded at the top by the Maximum Flooding Surface (MFS) and is overlain by the upward-shallowing Baishugou section, corresponding to the Highstand Systems Tract (HST; see Supplementary Information for further details on the study sites and samples).

Reconstructing ocean redox conditions at ca. 1.33 Ga

Molybdenum concentrations and isotopic compositions of organic-rich shales have been widely used as proxies for evaluating local and global oceanic redox conditions throughout Earth history[7,42–45]. The interpretation of Mo isotope ratios as a global-scale redox proxy is possible due to the long seawater residence time of Mo and near-quantitative drawdown of dissolved Mo in sediments deposited under strongly euxinic conditions[42,43]. The latter pathway results in reduced isotopic fractionations to near zero, whereas large fractionations may occur during Mo removal to oxic or anoxic, non-euxinic sediments[46,47]. A key caveat in these reconstructions is basin restriction, whereby in semi-restricted settings, rapid Mo drawdown into euxinic sediments may locally deplete dissolved Mo, suppressing sedimentary Mo enrichments and shifting $\delta^{98/95}$Mo values away from the open-ocean value[48]. Accordingly, Mo isotope values of euxinic black shales deposited in a basin connected to the open ocean are more likely to reflect the Mo isotope composition of the global ocean[49,50]. Under such conditions, changes in the Mo isotopic composition of seawater, as recorded by euxinic sediments, are thus indicative of global changes in the Mo budget, which are intrinsically linked to the evolution of redox conditions in ancient marine environments[45,47].

To determine whether Mo isotopic compositions of ancient marine sediments deposited under non-restricted conditions may represent the seawater composition requires initial consideration of local redox conditions. Iron speciation systematics and RSTE enrichment factors (EFs; see Methods for analytical details and Supplementary Information for a validation of our redox approach, as well as all data) are used here as proxies for local water-column redox conditions[51–53]. However, due to the high SiO_2 content of our samples (64–90%), we use a modified method to calculate enrichment

111 factors (EF^*; see Methods), which accounts for the dilution impact of chemical sedimentation on
112 the Al content of detrital sediments, which otherwise gives artificially elevated EFs[54,55]. Generally,
113 sedimentary enrichments in U, coupled with elevated highly reactive to total iron (Fe_{HR}/Fe_T) ratios
114 (>0.38), are indicative of deposition beneath an anoxic water-column[52,56,57]. Oxic conditions are
115 indicated by low Fe_{HR}/Fe_T (<0.22) and U_{EF}^* values, while Fe_{HR}/Fe_T from 0.22 to 0.38 are considered
116 equivocal[52]. For anoxic samples, low Mo_{EF}^* values and low pyrite (Fe_{py}) to Fe_{HR} ratios (<0.6)
117 indicate ferruginous water-column conditions, whereas elevated Mo_{EF}^* values and Fe_{py}/Fe_{HR} above
118 0.8 provide a strong indication of water-column euxinia, while Fe_{py}/Fe_{HR} between 0.6 and 0.8 are
119 considered potentially euxinic[52,56–58]. However, it should be noted that Mo enrichments may also
120 arise via uptake to Fe-Mn minerals, following mobilization of Fe^{2+} and Mn^{2+} under anoxic water-
121 column conditions and subsequent precipitation (commonly at the chemocline)[55,56]. This 'particulate
122 shuttle' mechanism for Mo drawdown can be evaluated by considering the combined behaviour of
123 Mo and U[55–57].

124 Our data document three sequential redox-controlled facies in the local redox evolution of the
125 Xiong'er Basin. In the Yutang section, Fe_{HR}/Fe_T values fluctuate from <0.22 to >0.38, with most
126 values falling in the equivocal zone, while U_{EF}^* values are somewhat elevated (>1), indicating minor
127 enrichment in the sediments (Fig. 1). In this section, Fe_{py}/Fe_{HR} values are consistently close to zero,
128 while Mo_{EF}^* values are only slightly elevated (Fig. 1). These combined signals suggest that the
129 redox state of bottom waters likely fluctuated, but were dominantly dysoxic (giving minor
130 enrichments in U as the sediments rapidly became anoxic on burial close to the sediment-water
131 interface). Under such conditions, Fe_{HR}/Fe_T data that fall in the equivocal and anoxic zones likely
132 record upwelling of anoxic ferruginous deeper waters[52,53]. Indeed, a Mo_{EF}^*–U_{EF}^* cross-plot (Fig. 2)
133 shows that the Yutang section samples generally plot between the particulate shuttle and redox
134 trajectory pathways, with the latter reflecting the progression from oxic through dysoxic to anoxic
135 conditions[54–56]. These data are consistent with drawdown of Mo in association with the precipitation
136 of Mn-oxides and Fe-(oxyhydr)oxides or green rust[59] close to the chemocline (i.e., the 'particulate
137 shuttle', giving Mo_{EF}^* values that plot above the redox trajectory), coupled with relatively minor
138 drawdown of U due to the development of anoxic porewaters close to the sediment-water interface
139 beneath a generally dysoxic water column[55,56].

In the Donggou'nao section, Fe_{HR}/Fe_T increases to values generally above 0.38, while Fe_{py}/Fe_{HR} remains low (until the uppermost sample), and there is a stepwise increase in U_{EF}^* and Mo_{EF}^* values relative to the Yutang section (Fig. 1). These data indicate the development of anoxic, ferruginous conditions in association with marine transgression. This is supported by Mo_{EF}^*–U_{EF}^* systematics (Fig. 2), where the data plot close to the anoxic, but non-euxinic field, with drawdown of Mo via uptake to Fe minerals precipitating in the ferruginous water-column again indicated. Likewise, a substantial increase in C_{org} content, from average values of 0.47 ± 0.43 wt% in the Yutang section to 7.61 ± 1.42 wt% in the Donggou'nao section (Fig. 1), is also consistent with the development of anoxic water-column conditions.

At the top of the Donggou'nao section, the increase in Fe_{py}/Fe_{HR} appears to document a transition to elevated values (>0.8) that persist throughout most of the Baishugou section (Fig. 1). Along with elevated Fe_{HR}/Fe_T values, this indicates a transition to persistent euxinia[52,53], which corresponds to a relative sea-level fall during deposition of the HST (note that this redox change begins in the Donggou'nao section and persists through the Baishugou section, and hence is not a consequence of sampling different sections). Under euxinic conditions, Fe^{2+} generated in porewaters is rapidly fixed in the sediments as Fe-sulphide minerals, preventing diffusion to the overlying water-column, and instead the sediments receive additional Fe_{HR} through Fe-sulphide formation in the water-column[60], giving elevated Fe_{HR}/Fe_T and Fe_{py}/Fe_{HR} values. The development of water-column euxinia is supported by persistently high Mo_{EF}^* values throughout the Baishugou section (Fig. 1), as well as Mo_{EF}^*–U_{EF}^* co-variation (Fig. 2). This interpretation is also consistent with sedimentological observations, specifically the presence of abundant small framboids with an average diameter of ~5 μm[61,62] (see Supplementary Information). Consistently elevated Mo concentrations and high Mo_{EF}^* values in the euxinic Baishugou section argue against deposition in a severely restricted basin, where rapid Mo drawdown would have suppressed sedimentary enrichments[48,57]. Instead, these enrichments, comparable to those in the open-marine Xiamaling Formation (Fig. 2), indicate efficient water exchange with the open ocean and a sustained supply of dissolved Mo. There is, however, a fall in Mo_{EF}^* and U_{EF}^* values in the top sample of the Donggou'nao section at the onset of persistent euxinia (Fig. 1). The reason for this is unclear, but may reflect transient, local drawdown of Mo and U from the water-column during the rapid

development of intensely euxinic conditions, before the subsequent resupply of these elements to the region through ocean circulation[54].

Having established the local redox regime in the Xiong'er Basin and the likelihood of open-marine depositional conditions, we next utilize Mo isotope values to track global changes in oxygenation. Although the data show some scatter, there is an overall progressive increase in both Mo contents and $\delta^{98/95}$Mo values upsection as the local redox conditions, in parallel with relative sea-level changes, evolved from dysoxic, through ferruginous, to euxinic (Figs. 1 and 3). Specifically, the dysoxic Yutang section has low and relatively invariant Mo contents (2.2 ± 2.5 ppm) and weakly negative to slightly positive $\delta^{98/95}$Mo values (–0.6 to +1.15‰), with an average of 0.32 ± 0.57‰. Molybdenum contents fluctuate considerably in the Donggou'nao section, but with an average value (17.5 ± 13.0 ppm) that is higher relative to the Yutang section, while the range in $\delta^{98/95}$Mo is also slightly shifted to more positive values (–0.47 to +1.29‰; average = 0.41 ± 0.52‰). In the Yutang and Donggou'nao sections, the wide range and relatively low $\delta^{98/95}$Mo values likely reflect a variable degree of Mo drawdown in association with Fe- and Mn-(oxyhydr)oxides, coupled with Mo cycling during diagenesis[47,49,63–65]. However, the most notable change is recorded by the Baishugou section, which has generally higher Mo contents (30.5 ± 17.8 ppm) and persistently positive $\delta^{98/95}$Mo values (+0.77 to +1.62‰; average = +1.24 ± 0.30‰). While euxinic conditions promote quantitative Mo removal, temporal fluctuations in dissolved H_2S concentration or the influence of the particulate Fe-Mn oxide shuttle, which preferentially delivers isotopically light Mo to sediments, can result in sedimentary $\delta^{98/95}$Mo values scattered over a relatively wide range, with values lower than that of contemporaneous seawater[64,66,67]. The highest $\delta^{98/95}$Mo value for the euxinic Baishugou section (+1.62‰) thus sets the minimum value for the $\delta^{98/95}$Mo composition of seawater at ca. 1.33 Ga[68].

The Mo isotope composition of black shales has played a pivotal role in identifying oxygenation events in the mid-Proterozoic[7,20,43,69,70]. However, $\delta^{98/95}$Mo records for the protracted interval of time encapsulated by the mid-Proterozoic remain scarce. It has been suggested that the seawater $\delta^{98/95}$Mo composition was in the range of 1.18 ± 0.12‰ from ca. 1.4 to 0.75 Ga[71]. Nevertheless, recent research has demonstrated higher $\delta^{98/95}$Mo values in marine sediments during mid-Proterozoic oxygenation events. For example, the ca. 1.56 Ga Gaoyuzhuang Formation in the NCC

documents an expanded range of Mo isotope values (–4.00 to +2.51‰), but rather than recording the seawater $\delta^{98/95}$Mo composition, these values have been linked to Fe and Mn redox shuttling in pore fluids[7]. By contrast, euxinic samples from the ca. 1.36 Ga Velkerri Formation in Australia have a maximum $\delta^{98/95}$Mo value of +1.17‰[14], while maximum $\delta^{98/95}$Mo values for euxinic samples of the ca. 1.40–1.35 Ga Xiamaling Formation are as high as +1.5 to +1.7‰[20]. In the latter case, the estimated seawater $\delta^{98/95}$Mo value during deposition of the Xiamaling Formation is +1.5‰ when samples with anomalously low Mo contents (<2 ppm) are excluded[18,20]. The high $\delta^{98/95}$Mo values for the Xiamaling Formation thus align with the suggestion that atmospheric oxygen may have been above 4% PAL at this time[11]. The $\delta^{98/95}$Mo values for the euxinic samples from the Baishugou Formation are even higher and constrain seawater $\delta^{98/95}$Mo to +1.62‰ at ca. 1.33 Ga (Figs. 1 and 3), consistent with a high degree of ocean (and potentially atmospheric) oxygenation.

Controls on the water-column redox structure

Phosphorus (P) is generally considered the ultimate biolimiting nutrient on geological timescales, and is thus a key element in controlling primary productivity, C_{org} burial, and consequently oxygen production[72–74]. The availability of P to fuel photosynthesis can be evaluated by considering the P content of marine sediments (here expressed as P/Al), in combination with consideration of molar C_{org}/P values relative to the Redfield ratio (106:1; noting that C_{org}/P represents minimum values relative to the Redfield C_{org}/P_{org}, due to the additional inclusion of detrital P phases in the total P measurement[54,71,75]). We utilize the C_{org}/P value not as a direct record of primary biomass stoichiometry, but as a proxy for the efficiency of sedimentary P retention versus recycling[75–77]. Phosphorus may undergo ‘sink switching’ during early diagenesis, whereby P may be mobilized during organic-matter degradation and the reductive dissolution of Fe (oxyhydr)oxides, followed by subsequent sequestration via repartitioning into authigenic phases (e.g., carbonate fluorapatite or vivianite) or re-adsorption to Fe (oxyhydr)oxides, if these phases persist closer to the sediment-water interface[78–81]. Critically, however, under anoxic conditions, particularly where the water-column or porewaters at the sediment-water interface are sulphidic, a portion of the remobilized P can be recycled back to the water-column, potentially triggering a positive productivity feedback[77,78,82].

In light of this framework, we first examine the relative supply of P to the sediments. P/Al values

are persistently highly elevated through the Baishugou Formation, relative to the average value of 0.009 for upper continental crust[83] (Fig. 1), indicating a sedimentary phosphorus reservoir substantially enriched relative to the detrital background. This implies an enhanced external influx of P (e.g., via continental weathering) that helped to promote reducing water-column conditions.

To evaluate redox controls on P cycling, we next consider C_{org}/P ratios. The trend in C_{org}/P ratios through the Baishugou Formation documents secular variability in P recycling back to the water-column (Fig. 1). Under dysoxic conditions, C_{org}/P values are well below the Redfield ratio, suggesting effective trapping of P in the sediment. By contrast, under ferruginous conditions C_{org}/P values fall close to the Redfield ratio. Given that these are minimum values, this suggests some degree of P recycling back to the water-column[84,85], which is consistent with the increased Fe_{py}/Fe_{HR} (suggesting enhanced, porewater sulphide generation) for this interval[54,74,78,84] (Fig. 1). Under euxinic conditions, C_{org}/P values are particularly high (up to 791:1), suggesting effective recycling of phosphate back to the water-column. This would have maintained high rates of organic productivity, regardless of whether the region received a substantial influx of phosphate from terrestrial weathering. In turn, this would have increased the depositional flux of C_{org}, helping to maintain euxinic conditions via microbial reduction of sulphate. The subsequent increase in the burial of both organic matter and pyrite would have driven increased oxygen buildup in surface environments[86,87].

The observed coupling between redox state and nutrient cycling efficiency provides the foundation for a schematic model (Fig. 3) depicting a stable oxygen-minimum zone (OMZ) in the Xiong'er Basin at ca. 1.33 Ga. This model tracks the migration of the redox-controlled facies with sea level change (see Supplementary Information) across the region. Specifically, the Yutang section was deposited in relatively shallower, dysoxic waters during the initial TST. With sea-level rise culminating at the MFS, the Donggou'nao section was deposited in the deeper, ferruginous core of the OMZ. Subsequently, the Baishugou section, deposited during the HST, indicates shallowing conditions as the sampling site moved out of the ferruginous core and into the overlying, euxinic wedge. While this overall redox-stratification was likely persistent during deposition of the Baishugou Formation, the boundaries of the OMZ were likely dynamic in intensity and extent, consistent with observations in other Mesoproterozoic settings[11,52,88]. This long-term redox-

stratification exerted a key control on biogeochemical cycles, whereby the establishment of euxinia facilitated efficient phosphorus recycling, which, in turn, supported high productivity and enhanced organic carbon burial, and ultimately contributed to the release of oxygen to surface waters.

Protracted oxygenation between ca. 1.4 and 1.3 Ga

Evidence from the ca. 1.40–1.35 Ga Xiamaling and ca. 1.42–1.36 Ga Velkerri formations indicates at least episodically enhanced oxygenation during the 1.42–1.35 Ga interval[20,30,40,41,89]. Our data for the ca. 1.33 Ga Baishugou Formation builds upon this, indicating protracted enhancement of ocean oxygenation in the early Ectasian, until at least ca. 1.33 Ga. Collectively, these formations establish a robust chronostratigraphic framework for evaluating redox conditions across the 1.4–1.3 Ga period (see Fig. 4 and Supplementary Information). Enhanced and protracted oxygenation is further corroborated by elevated Mo isotope values in all three formations, indicating pervasive, global oxygenation and an increased seawater Mo inventory[14,20] (Fig. 3). In addition, high C_{org} and P contents in all three units support abundant nutrient availability and enhanced organic matter burial[14,30,41,89] (see Fig. 4d and Supplementary Information).

Ocean euxinia would have enhanced water-column phosphorus availability, boosting primary productivity and respiration through a short-term positive feedback and potentially depleting dissolved oxygen locally[90]. However, organic carbon burial would have ultimately contributed to atmospheric and ocean oxygenation[91], with euxinic conditions leading to particularly enhanced organic matter burial[92,93] (Fig. 3). Consequently, this scenario implies that the early Ectasian (1.4–1.3 Ga) was generally characterized by relatively high atmospheric (>4% PAL) and oceanic oxygen levels. These conditions allowed for the expansion of oxygenated, redox-stable shallow-marine environments conducive to eukaryotic evolution, as evidenced by microfossils in the Xiamaling and Velkerri formations[35,94]. However, despite its duration, mid-Proterozoic oxygenation was likely limited in amplitude and did not profoundly impact the carbon cycle, as major carbon isotope excursions are absent during this period[5].

Conclusions

Our high-resolution reconstruction of redox conditions and nutrient cycling in the ca. 1.33 Ga

Baishugou Formation on the southern margin of the NCC provides evidence for the development on the outer- to inner-shelf of a stable, oxygen-minimum zone, with a euxinic to ferruginous core surrounded by dysoxic to oxic waters. Critically, euxinic and ferruginous conditions led to enhanced P recycling and increased C_{org} burial, with highly positive $\delta^{98/95}$Mo values (up to +1.62‰) recorded under euxinic conditions, indicative of expanded ocean oxygenation. When placed in the context of existing Mesoproterozoic surface redox records, our results extend evidence for elevated ocean oxygenation to ca. 1.33 Ga, suggesting that the early Ectasian (ca. 1.4–1.3 Ga) was a protracted period with generally elevated seawater oxygen levels. This long-lasting stability of oxygenated marine conditions could have readily facilitated the diversification of early eukaryotes.

Methods

Elemental Geochemistry

Major element concentrations were determined by wavelength-dispersive X-ray fluorescence (XRF; Rigaku ZSX100e). Whole-rock powders (~0.5 g) were fused with $Li_2B_4O_7$ flux to prepare glass disks, with analytical precision verified using international standards BHVO-2 and AGV-2 (RSD ≤5%; SiO_2 ± 1%, MnO and Fe_2O_3 ± 5%, other oxides ± 2%). Trace elements (Mn, Mo, Sr) were analyzed via inductively coupled plasma mass spectrometry (ICP-MS; Agilent 7700x). Samples were digested in high-pressure Teflon bombs with HNO_3 and HF (195°C, 24 h), calibrated against W-2, AGV-2, BHVO-2 and GSP-2 standards (<10% deviation from certified values). Elemental analyses were conducted at the Sample Solution Laboratory (Wuhan, China) and Nanjing Hongchuang Laboratory (Nanjing, China).

Trace Metal Enrichment Factors

A revised approach[54] was taken to calculate enrichment factors (EF^*) to account for a high degree of detrital sediment dilution by silica. Excess element concentrations were derived as:

$$Element_{excess} = Element_{sample} - \left(Al_{sample} \times \frac{Element_{UCC}}{Al_{UCC}}\right) \quad (1)$$

EF^* was then defined using upper continental crust (UCC) reference values[95]:

$$Element_{EF*} = \frac{Element_{excess} + Element_{UCC}}{Element_{UCC}} \quad (2)$$

Iron Speciation Analyses

Sequential extractions were conducted at Nanjing Hongchuang Laboratory (Nanjing, China) to quantify sulfide-reactive Fe phases[51]. Carbonate-bound Fe (Fe_{carb}) was extracted with 1 M sodium acetate (pH 4.5, 48 h), oxide-bound Fe (Fe_{ox}) was extracted with citrate-dithionite (2 h), and magnetite Fe was extracted by sodium oxalate (6 h). Pyrite Fe (Fe_{py}) was determined separately via chromium reduction[96]. The highly reactive Fe (Fe_{HR}) pool was calculated as $Fe_{HR} = Fe_{carb} + Fe_{ox} + Fe_{mag} + Fe_{py}$. Iron concentrations for the sequential steps were measured by ICP-MS (Agilent 7500ce; reproducibility ±7%, n = 12 replicates), while Fe_{py} was determined gravimetrically via precipitation as Ag_2S.

Total Organic Carbon Analyses

Total organic carbon analyses were performed at Nanjing Hongchuang Laboratory (Nanjing, China), using a LECO CS-344 analyzer. Samples were decarbonated with 1 M HCl, rinsed to pH >4 with ultrapure water, and combusted at 1050°C. Precision was validated against IFP160000 reference material (RSD <5%).

Molybdenum Isotope Analyses

Molybdenum isotope analyses were performed on samples with Mo concentrations >50 ppb at the State Key Laboratory of Isotope Geochemistry, Guangzhou Institute of Geochemistry, Chinese Academy of Sciences. Mo was separated and purified after whole-rock dissolution using N-benzoyl-N-phenylhydroxylamine (BPHA) resin (0.3–0.5 mL) following established protocols[97]. The isotopic composition of Mo was expressed as $\delta^{98/95}$Mo relative to the NIST SRM 3134 standard, and the ratios were measured on a Thermo Fisher Scientific Neptune Plus multicollector-inductively coupled plasma mass-spectrometer (MC-ICP-MS). Instrumental mass fractionation during the Mo isotope analyses was corrected using the double dilution method[97]. During the same analytical sessions when the samples were analyzed, solutions of the NIST-SRM-3134 standard and the seawater standard yielded $\delta^{98/95}$Mo values of 0.00 ± 0.06‰ (2SD, n = 31) and 2.08 ± 0.04‰ (2SD, n = 4), respectively. The procedural blank had 0.12 ± 0.01 ng Mo (2SD, n = 3), far less than the total Mo content of the samples. Values of $\delta^{98/95}$Mo for the samples relative to NIST SRM 3134 ($\delta^{98/95}$Mo = 0.25‰) were calculated as follows[98]:

$$\delta^{98/95}\text{Mo}\ (‰) = \left(\frac{(^{98/95}\text{Mo})_{\text{sample}}}{(^{98/95}\text{Mo})_{\text{NIST3134}} * 0.99975} - 1 \right) \times 1000 \quad (3)$$

Data Availability Statement

Supplementary information and Supplementary data (Table S1-S6) have been deposited in https://doi.org/10.5281/zenodo.19696616.

References

1. Farquhar, J., Bao, H. & Thiemens, M. Atmospheric influence of Earth's earliest sulfur cycle. *Science* **289**, 756–758 (2000).
2. Bekker, A. *et al.* Dating the rise of atmospheric oxygen. *Nature* **427**, 117–120 (2004).
3. Och, L. M. & Shields-Zhou, G. A. The Neoproterozoic oxygenation event: environmental perturbations and biogeochemical cycling. *Earth Sci. Rev.* **110**, 26–57 (2012).
4. Krause, A. J. *et al.* Stepwise oxygenation of the Paleozoic atmosphere. *Nat. Commun.* **9**, 4081 (2018).
5. Prokoph, A., Shields, G. A. & Veizer, J. Compilation and time-series analysis of a marine carbonate δ^{18}O, δ^{13}C, ^{87}Sr/^{86}Sr and δ^{34}S database through Earth history. *Earth-Science Reviews* **87**, 113–133 (2008).
6. Zhang, K. *et al.* Oxygenation of the Mesoproterozoic ocean and the evolution of complex eukaryotes. *Nat. Geosci.* **11**, 345–350 (2018).
7. Luo, J. *et al.* Pulsed oxygenation events drove progressive oxygenation of the early Mesoproterozoic ocean. *Earth Planet. Sci. Lett.* **559**, 116754 (2021).
8. Tang, D. *et al.* Terminal Mesoproterozoic (1.1–1.0 Ga) shallow ocean oxygenation and the rise of crown-group eukaryotes. *GSA Bull.* **137**, 3452–3462 (2025).
9. Planavsky, N. J. *et al.* Low mid-Proterozoic atmospheric oxygen levels and the delayed rise of animals. *Science* **346**, 635–638 (2014).
10. Cole, D. B. *et al.* A shale-hosted Cr isotope record of low atmospheric oxygen during the Proterozoic. *Geology* **44**, 555–558 (2016).
11. Zhang, S. *et al.* Sufficient oxygen for animal respiration 1,400 million years ago. *Proc. Natl. Acad. Sci. U.S.A.* **113**, 1731–1736 (2016).
12. Zhang, S. *et al.* The oxic degradation of sedimentary organic matter 1400 Ma constrains atmospheric oxygen

levels. *Biogeosciences* **14**, 2133–2149 (2017).

13. Canfield, D. E. *et al.* Highly fractionated chromium isotopes in Mesoproterozoic-aged shales and atmospheric oxygen. *Nat. Commun.* **9**, 1–11 (2018).

14. Kendall, B., Creaser, R. A., Gordon, G. W. & Anbar, A. D. Re–Os and Mo isotope systematics of black shales from the middle Proterozoic Velkerri and Wollogorang Formations, McArthur Basin, northern Australia. *Geochim. Cosmochim. Acta* **73**, 2534–2558 (2009).

15. Shi, Q. *et al.* Heterogeneous oxygenation coupled with low phosphorus bio-availability delayed eukaryotic diversification in Mesoproterozoic oceans: evidence from the ca 1.46 Ga Hongshuizhuang Formation of North China. *Precambrian Res.* **354**, 106050 (2021).

16. Ma, K. *et al.* Sedimentary environments and mechanisms of organic matter enrichment in the Mesoproterozoic Hongshuizhuang Formation of northern China. *Palaeogeogr. Palaeoclimatol. Palaeoecol.* **475**, 176–187 (2017).

17. Canfield, D. E. *et al.* A Mesoproterozoic iron formation. *Proc. Natl. Acad. Sci. U.S.A.* **115**, E3895–E3904 (2018).

18. Zhang, S., Wang, H., Wang, X. & Ye, Y. The Mesoproterozoic oxygenation event. *Sci. China Earth Sci.* **64**, 2043–2068 (2021).

19. Xu, L. *et al.* Shallow seawater oxygenation at ca. 1.44 Ga: a reflection of local seafloor oxygen oases or extensive water-column oxygenation? *GSA Bull.* https://doi.org/10.1130/B38041.1 (2025) doi:10.1130/B38041.1.

20. Zhang, S. *et al.* Paleoenvironmental proxies and what the Xiamaling Formation tells us about the mid-Proterozoic ocean. *Geobiology* **17**, 225–246 (2019).

21. Yang, S., Kendall, B., Lu, X., Zhang, F. & Zheng, W. Uranium isotope compositions of mid-proterozoic black shales: evidence for an episode of increased ocean oxygenation at 1.36 Ga and evaluation of the effect of post-depositional hydrothermal fluid flow. *Precambrian Res.* **298**, 187–201 (2017).

22. Shang, M. *et al.* A pulse of oxygen increase in the early Mesoproterozoic ocean at *ca*. 1.57–1.56 Ga. *Earth Planet. Sci. Lett.* **527**, 115797 (2019).

23. Yang, X. *et al.* Pulse of intense oxidative weathering during the latest Paleoproterozoic. *Geology* **53**, 78–82 (2025).

24. Hardisty, D. S. *et al.* Perspectives on Proterozoic surface ocean redox from iodine contents in ancient and recent carbonate. *Earth Planet. Sci. Lett.* **463**, 159–170 (2017).

25. Song, Y. *et al.* Tracking the spatial extent of redox variability in the mid-Proterozoic ocean. *Geology* https://doi.org/10.1130/G53447.1 (2025) doi:10.1130/G53447.1.

26. Diamond, C. W., Planavsky, N. J., Wang, C. & Lyons, T. W. What the 1.4 Ga Xiamaling Formation can and cannot tell us about the mid-Proterozoic ocean. *Geobiology* **16**, 219–236 (2018).

27. Evans, D. A. D. & Mitchell, R. N. Assembly and breakup of the core of Paleoproterozoic–Mesoproterozoic supercontinent Nuna. *Geology* **39**, 443–446 (2011).

28. Zhang, S.-H. *et al.* Spatial distribution of 1.4-1.3 Ga LIPs and carbonatite-related REE deposits: Evidence for large-scale continental rifting in the Columbia (Nuna) supercontinent. *Earth Planet. Sci. Lett.* **597**, 117815 (2022).

29. Mitchell, R. N., Kirscher, U., Kunzmann, M., Liu, Y. & Cox, G. M. Gulf of Nuna: Astrochronologic correlation of a Mesoproterozoic oceanic euxinic event. *Geology* **49**, 25–29 (2021).

30. Mukherjee, I. & Large, R. R. Pyrite trace element chemistry of the Velkerri Formation, Roper Group, McArthur Basin: evidence for atmospheric oxygenation during the Boring Billion. *Precambrian Res.* **281**, 13–26 (2016).

31. Su, W. *et al.* SHRIMP U–Pb ages of K-bentonite beds in the Xiamaling Formation: implications for revised subdivision of the Meso- to Neoproterozoic history of the North China Craton. *Gondwana Res.* **14**, 543–553 (2008).

32. Su, W. *et al.* SHRIMP U-Pb dating for a K-bentonite bed in the Tieling Formation, North China. *Chin. Sci. Bull.* **55**, 3312–3323 (2010).

33. Li, H. *et al.* Recent advances in the study of the Mesoproterozoic geochronology in the North China Craton. *Journal of Asian Earth Sciences* **72**, 216–227 (2013).

34. Zhu, X. *et al.* Zircon U-Pb geochronology of tuffite beds in the Baishugou Formation: constraints on the revision of Ectasian system at the southern margin of the North China Craton. *Sci. China Earth Sci.* **63**, 1817–1830 (2020).

35. Miao, L., Moczydłowska, M. & Zhu, M. A diverse organic-walled microfossil assemblage from the Mesoproterozoic Xiamaling Formation, North China. *Precambrian Res.* **360**, 106235 (2021).

36. Zhao, T. *et al.* Zircon U-Pb SHRIMP dating for the volcanic rocks of the Xiong'er group: constraints on the initial formation age of the cover of the North China Craton. *Chin. Sci. Bull.* **49**, 2495–2502 (2004).

37. Zhai, M., Hu, B., Zhao, T., Peng, P. & Meng, Q. Late Paleoproterozoic–Neoproterozoic multi-rifting events

422 in the North China Craton and their geological significance: a study advance and review. *Tectonophysics* **662**,
423 153–166 (2015).
424 38. Su, W. Revision of the Mesoproterozoic chronostratigraphic subdivision both of the North China and Yangtze
425 Cratons and the relevant issues. *Earth Sci. Front.* **23**, 156–185 (2016), in Chinese with English abstract.
426 39. Gao, L. *et al.* Zircon SHRIMP U-Pb dating of the tuff bed in the Xiamaling Formation of the Qingbaikouan
427 System in North China. *Geol. Bull. China* **26**, 249–255 (2007), in Chinese with English abstract.
428 40. Zhang, S. *et al.* Orbital forcing of climate 1.4 billion years ago. *Proc. Natl. Acad. Sci. U.S.A.* **112**, E1406–
429 E1413 (2015).
430 41. Yang, X. *et al.* Mafic magmatism triggered the Mesoproterozoic oxygenation event: Re-Os-PGE evidence
431 from the Xiamaling Formation in North China and Velkerri Formation in North Australia. *Earth Planet. Sci. Lett.*
432 **667**, 119512 (2025).
433 42. Siebert, C., Nägler, T. F., von Blanckenburg, F. & Kramers, J. D. Molybdenum isotope records as a potential
434 new proxy for paleoceanography. *Earth Planet. Sci. Lett.* **211**, 159–171 (2003).
435 43. Arnold, G. L., Anbar, A. D., Barling, J. & Lyons, T. W. Molybdenum isotope evidence for widespread anoxia
436 in mid-Proterozoic oceans. *Science* **304**, 87–90 (2004).
437 44. Dickson, A. J. A molybdenum-isotope perspective on Phanerozoic deoxygenation events. *Nat. Geosci.* **10**,
438 721–726 (2017).
439 45. Asael, D., Rouxel, O., Poulton, S. W., Lyons, T. W. & Bekker, A. Molybdenum record from black shales
440 indicates oscillating atmospheric oxygen levels in the early Paleoproterozoic. *Am. J. Sci.* **318**, 275–299 (2018).
441 46. Morford, J. L. & Emerson, S. The geochemistry of redox-sensitive trace metals in sediments. *Geochim.*
442 *Cosmochim. Acta* **63**, 1735–1750 (1999).
443 47. Siebert, C., McManus, J., Bice, A., Poulson, R. & Berelson, W. M. Molybdenum isotope signatures in
444 continental margin marine sediments. *Earth Planet. Sci. Lett.* **241**, 723–733 (2006).
445 48. Algeo, T. J. & Lyons, T. W. Mo–total organic carbon covariation in modern anoxic marine environments:
446 Implications for analysis of paleoredox and paleohydrographic conditions. *Paleoceanography* **21**, 2004PA001112
447 (2006).
448 49. Barling, J., Arnold, G. L. & Anbar, A. D. Natural mass-dependent variations in the isotopic composition of
449 molybdenum. *Earth Planet. Sci. Lett.* **193**, 447–457 (2001).
450 50. Emerson, S. R. & Huested, S. S. Ocean anoxia and the concentrations of molybdenum and vanadium in

seawater. *Mar. Chem.* **34**, 177–196 (1991).

51. Poulton, S. W. & Canfield, D. E. Development of a sequential extraction procedure for iron: implications for iron partitioning in continentally derived particulates. *Chem. Geol.* **214**, 209–221 (2005).

52. Poulton, S. W. & Canfield, D. E. Ferruginous conditions: A dominant feature of the ocean through Earth's History. *Elements* **7**, 107–112 (2011).

53. Poulton, S. W. *The Iron Speciation Paleoredox Proxy*. (Cambridge University Press, 2021).

54. Krewer, C. *et al.* Controls on the termination of Cretaceous Oceanic Anoxic Event 2 in the Tarfaya Basin, Morocco. *Am. J. Sci.* **324,** 11 (2024).

55. Li, S., Wignall, P. B. & Poulton, S. W. Co-application of rhenium, vanadium, uranium and molybdenum as paleo-redox proxies: insight from modern and ancient environments. *Chem. Geol.* **674**, 122565 (2025).

56. Tribovillard, N., Algeo, T. J., Lyons, T. & Riboulleau, A. Trace metals as paleoredox and paleoproductivity proxies: An update. *Chem. Geol.* **232**, 12–32 (2006).

57. Algeo, T. J. & Tribovillard, N. Environmental analysis of paleoceanographic systems based on molybdenum–uranium covariation. *Chem. Geol.* **268**, 211–225 (2009).

58. Poulton, S. W. *et al.* A 200-million-year delay in permanent atmospheric oxygenation. *Nature* **592**, 232–236 (2021).

59. Zegeye, A. *et al.* Green rust formation controls nutrient availability in a ferruginous water column. *Geology* **40**, 599–602 (2012).

60. Canfield, D. E., Lyons, T. W. & Raiswell, R. A model for iron deposition to euxinic Black Sea sediments. *Am. J. Sci.* **296**, 818–834 (1996).

61. Wilkin, R. T., Barnes, H. L. & Brantley, S. L. The size distribution of framboidal pyrite in modern sediments: an indicator of redox conditions. *Geochim. Cosmochim. Acta* **60**, 3897–3912 (1996).

62. Wignall, P. B. & Newton, R. Pyrite framboid diameter as a measure of oxygen deficiency in ancient mudrocks. *Am. J. Sci.* **298**, 537–552 (1998).

63. Poulson Brucker, R. L., McManus, J., Severmann, S. & Berelson, W. M. Molybdenum behavior during early diagenesis: insights from Mo isotopes. *Geochem. Geophys. Geosyst.* **10**, Q06010 (2009).

64. Goldberg, T., Archer, C., Vance, D. & Poulton, S. W. Mo isotope fractionation during adsorption to Fe (oxyhydr)oxides. *Geochim. Cosmochim. Acta* **73**, 6502–6516 (2009).

65. Goldberg, T. *et al.* Controls on Mo isotope fractionations in a Mn-rich anoxic marine sediment, Gullmar

480 Fjord, Sweden. *Chem. Geol.* **296–297**, 73–82 (2012).
481 66. Neubert, N., Nägler, T. F. & Böttcher, M. E. Sulfidity controls molybdenum isotope fractionation into euxinic
482 sediments: Evidence from the modern Black Sea. *Geology* **36**, 775–778 (2008).
483 67. Nägler, T. F., Neubert, N., Böttcher, M. E., Dellwig, O. & Schnetger, B. Molybdenum isotope fractionation
484 in pelagic euxinia: Evidence from the modern Black and Baltic Seas. *Chem. Geol.* **289**, 1–11 (2011).
485 68. Kendall, B. *et al.* Inverse correlation between the molybdenum and uranium isotope compositions of upper
486 Devonian black shales caused by changes in local depositional conditions rather than global ocean redox variations.
487 *Geochim. Cosmochim. Acta* **287**, 141–164 (2020).
488 69. Xu, D. *et al.* Extensive sea-floor oxygenation during the early Mesoproterozoic. *Geochim. Cosmochim. Acta*
489 **354**, 186–196 (2023).
490 70. Ye, Y. *et al.* Black shale Mo isotope record reveals dynamic ocean redox during the Mesoproterozoic Era.
491 *Geochem. Persp. Let.* **18**, 16–21 (2021).
492 71. Guilbaud, R. *et al.* Phosphorus-limited conditions in the early Neoproterozoic ocean maintained low levels
493 of atmospheric oxygen. *Nat. Geosci.* **13**, 296–301 (2020).
494 72. Tyrrell, T. The relative influences of nitrogen and phosphorus on oceanic primary production. *Nature* **400**,
495 525–531 (1999).
496 73. Algeo, T. J. & Ingall, E. Sedimentary C_{org}:P ratios, paleo-ocean ventilation, and Phanerozoic atmospheric
497 pO_2. *Palaeogeogr. Palaeoclimatol. Palaeoecol.* **256**, 130–155 (2007).
498 74. Reinhard, C. T. *et al.* Evolution of the global phosphorus cycle. *Nature* **541**, 386–389 (2017).
499 75. Qiu, Z. *et al.* A nutrient control on expanded anoxia and global cooling during the late Ordovician mass
500 extinction. *Commun. Earth Environ.* **3**, 82 (2022).
501 76. Ingall, E. D., Bustin, R. M. & Van Cappellen, P. Influence of water column anoxia on the burial and
502 preservation of carbon and phosphorus in marine shales. *Geochim. Cosmochim. Acta* **57**, 303–316 (1993).
503 77. Ingall, E. & Jahnke, R. Evidence for enhanced phosphorus regeneration from marine sediments overlain by
504 oxygen-depleted waters. *Geochim. Cosmochim. Acta* **58**, 2571–2575 (1994).
505 78. Alcott, L. J., Mills, B. J. W., Bekker, A., & Poulton, S. W. Earth's great oxidation event facilitated by the rise
506 of sedimentary phosphorus recycling. *Nat. Geosci.* **15**, 210–215 (2022).
507 79. Krom, M. D. & Berner, R. A. The diagenesis of phosphorus in a nearshore marine sediment. *Geochim.*
508 *Cosmochim. Acta* **45**, 207–216 (1981).

509 80. Slomp, C. P., Epping, E. H. G., Helder, W. & Raaphorst, W. V. A key role for iron-bound phosphorus in
510 Authigenic apatite Formation in North Atlantic continental platform sediments. *J. Mar. Res.* **54**, 1179–1205 (1996).
511 81. Ruttenberg, K. C. & Berner, R. A. Authigenic apatite Formation and burial in sediments from non-upwelling,
512 continental margin environments. *Geochim. Cosmochim. Acta* **57**, 991–1007 (1993).
513 82. Ingall, E. & Jahnke, R. Influence of water-column anoxia on the elemental fractionation of carbon and
514 phosphorus during sediment diagenesis. *Mar. Geol.* **139**, 219–229 (1997).
515 83. McLennan, S. M. Relationships between the trace element composition of sedimentary rocks and upper
516 continental crust. *Geochem. Geophys. Geosyst.* **2**, 2000GC000109 (2001).
517 84. Xiong, Y. *et al.* Phosphorus cycling in Lake Cadagno, Switzerland: a low sulfate euxinic ocean analogue.
518 *Geochim. Cosmochim. Acta* **251**, 116–135 (2019).
519 85. Yang, X. *et al.* A phosphate-rich marine reservoir in the redox stratified Ediacaran ocean. *Commun. Earth*
520 *Environ.* **5**, 41 (2024).
521 86. Canfield, D. E. A new model for Proterozoic ocean chemistry. *Nature* **396**, 451–453 (1998).
522 87. Lyons, T. W., Reinhard, C. T. & Planavsky, N. J. The rise of oxygen in Earth's early ocean and atmosphere.
523 *Nature* **506**, 307–315 (2014).
524 88. Song, Y. *et al.* Dynamic redox and nutrient cycling response to climate forcing in the Mesoproterozoic ocean.
525 *Nat. Commun.* **14**, 6640 (2023).
526 89. Xu, L. *et al.* Large igneous province emplacement triggered an oxygenation event at ~1.4 Ga: Evidence from
527 mercury and paleo-productivity proxies. *Geophysical Research Letters* **51**, e2023GL106654 (2024).
528 90. Van Cappellen, P. & Ingall, E. D. Benthic phosphorus regeneration, net primary production, and ocean anoxia:
529 a model of the coupled marine biogeochemical cycles of carbon and phosphorus. *Paleoceanography* **9**, 677–692
530 (1994).
531 91. Daines, S. J., Mills, B. J. W. & Lenton, T. M. Atmospheric oxygen regulation at low Proterozoic levels by
532 incomplete oxidative weathering of sedimentary organic carbon. *Nat. Commun.* **8**, 14379 (2017).
533 92. Raven, M. R., Sessions, A. L., Adkins, J. F. & Thunell, R. C. Rapid organic matter sulfurization in sinking
534 particles from the Cariaco Basin water column. *Geochim. Cosmochim. Acta* **190**, 175–190 (2016).
535 93. Raven, M. R., Keil, R. G. & Webb, S. M. Microbial sulfate reduction and organic sulfur formation in sinking
536 marine particles. *Science* **371**, 178–181 (2021).
537 94. Javaux, E. J., Knoll, A. H. & Walter, M. R. TEM evidence for eukaryotic diversity in mid-Proterozoic oceans.

538 *Geobiology* **2**, 121–132 (2004).
539 95. Rudnick, R. L. & Gao, S. Composition of the Continental Crust. in *Treatise on Geochemistry* 1–64 (Elsevier,
540 2003). doi:10.1016/B0-08-043751-6/03016-4.
541 96. Canfield, D. E., Raiswell, R., Westrich, J. T., Reaves, C. M. & Berner, R. A. The use of chromium reduction
542 in the analysis of reduced inorganic sulfur in sediments and shales. *Chem. Geol.* **54**, 149–155 (1986).
543 97. Li, J. *et al.* Measurement of the isotopic composition of molybdenum in geological samples by MC-ICP-MS
544 using a novel chromatographic extraction technique. *Geostand. Geoanal. Res.* **38**, 345–354 (2014).
545 98. Nägler, T. F. *et al.* Proposal for an international molybdenum isotope measurement standard and data
546 representation. *Geostand. Geoanal. Res.* **38**, 149–151 (2014).
547 99. Wang, X. *et al.* Oxygen, climate and the chemical evolution of a 1400 million year old tropical marine setting.
548 *Am. J. Sci.* **317**, 861–900 (2017).
549

Competing Interests

The authors declare no competing interests.

Author Contributions

X. Zhu and C. Jia designed the research and prepared the original manuscript. W. Su, X. Zhu and C. Jia measured sections, performed comprehensive sedimentary facies analysis and collected samples. C. Jia and X. Zhu performed analyses. C. Jia, X. Zhu, A. Bekker and S.W. Poulton interpreted the geochemical data. C. Jia, X. Zhu, A. Bekker, S.W. Poulton, W. Su and T. Zhao wrote the manuscript.

Funding

This study was financially supported by the National Key Research and Development Project of China (No. 2025ZD1005300, No. 2020YFA0714803), the National Natural Science Foundation of China (No. 42572246) and the Research Project of State Key Laboratory of Lithospheric and Environmental Coevolution (No. SKL-K202402).

Acknowledgements

We thank Prof. Jie Li for his expertise and assistance in conducting the molybdenum isotope analyses. We are grateful to Shiyan Wang, Shuqi Liu and Yuhong Fan for their invaluable effort and collaboration during field discussions and sample collection. We also appreciate helpful discussions with Xiqiang Zhou, Mingshuai Zhu and Run Li.

Figures

Figure 1. Geochemical profiles for the Baishugou Formation, showing Fe_{HR}/Fe_T, Fe_{py}/Fe_{HR}, Mo_{EF}^*, U_{EF}^*, C_{org}, P/Al, C_{org}/P, Mo contents and $\delta^{98/95}Mo$. The dashed orange line represents the average P/Al value of 0.009 for upper continental crust (UCC)[83]. A molar C/P of 106:1 denotes the Redfield ratio (blue dashed line). The age data are adopted from ref.[34]. MFS–Maximum Flooding Surface; TST–Transgressive Systems Tract; HST–Highstand Systems Tract.

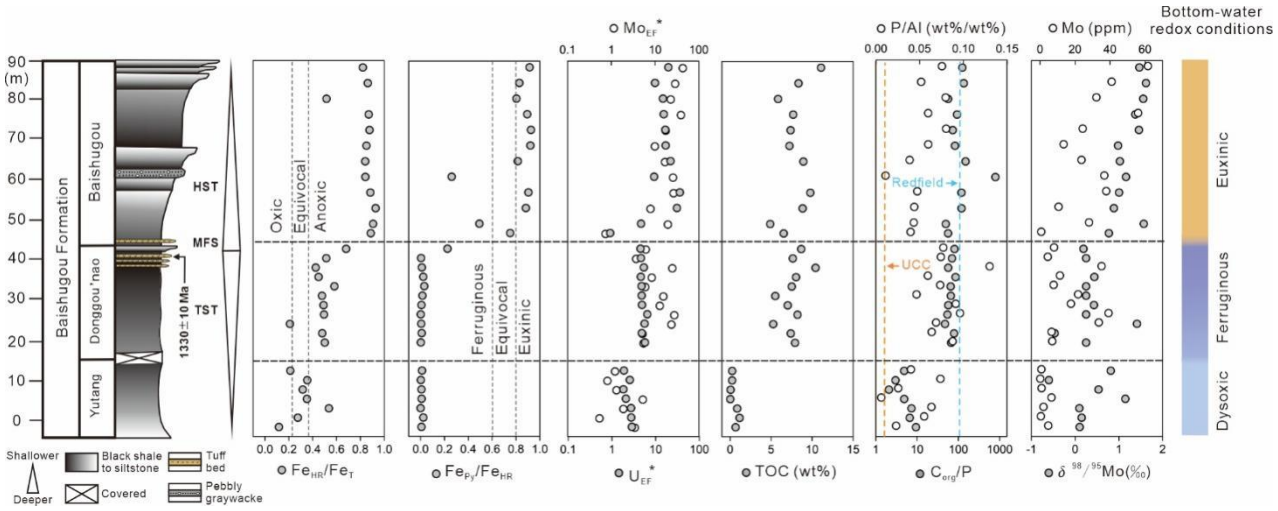

Figure 2. Mo_{EF}^{*}–U_{EF}^{*} crossplot for the Baishugou Formation. The circles represent data from the three sections of the Baishugou Formation, whereas the grey crosses denote data from the open-marine Xiamaling Formation (data from ref[99]). Dotted lines indicate RSTEs accumulation pathways, whereby the 'particulate shuttle' represents Mo uptake associated with the water-column precipitation of Fe- and Mn-(oxyhydr)oxides, and the 'redox variation' trajectory reflects dysoxic through anoxic to euxinic water-column conditions. The diagonal lines represent multiplication factors (0.1, 0.3 and 1) of the Mo/U value for present-day seawater[57].

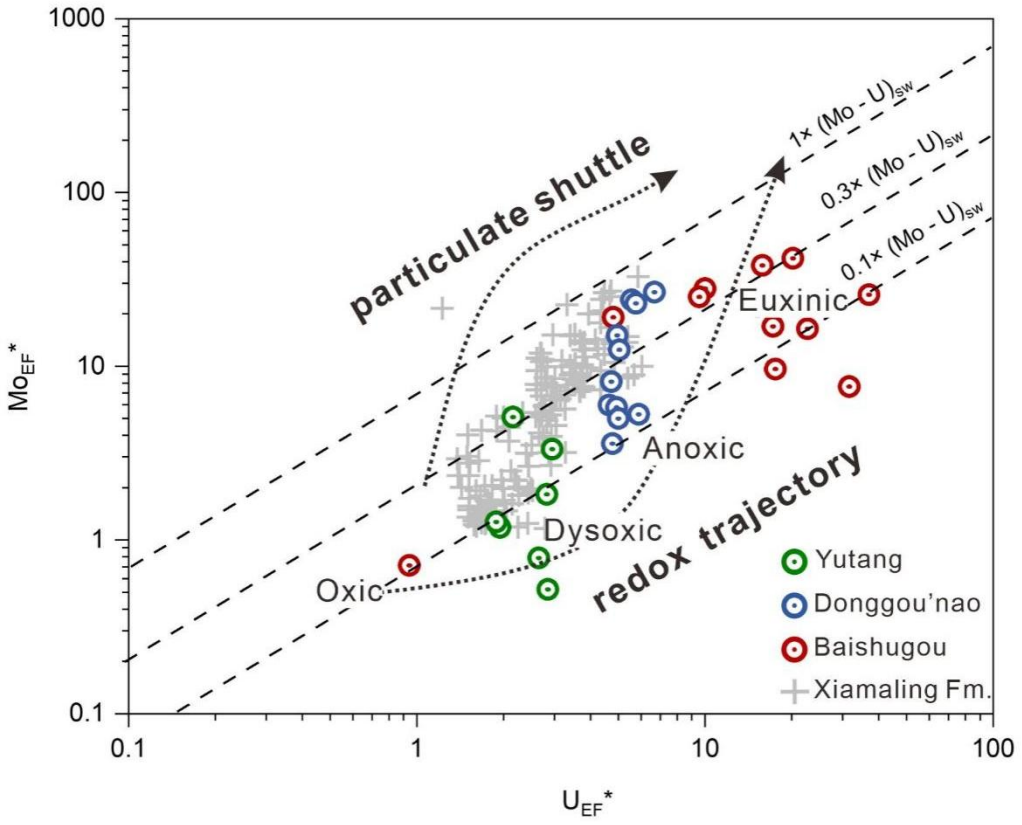

Figure 3. Schematic representation of redox stratification in the Xiong'er Basin during deposition of the Baishugou Formation. An oxygen-minimum zone (OMZ) redox structure is shown at the top, and simplified relative sea level changes, recorded by the stratigraphic sections, are shown at the bottom left. The redox structure is characterized by a central zone of dynamic euxinic to ferruginous conditions, flanked by dysoxic to oxic environments developed across the outer- to inner-shelf, which modulated phosphorus recycling and organic carbon burial. Dashed lines refer to redox boundaries and double-pointing arrows indicate redoxcline fluctuations.

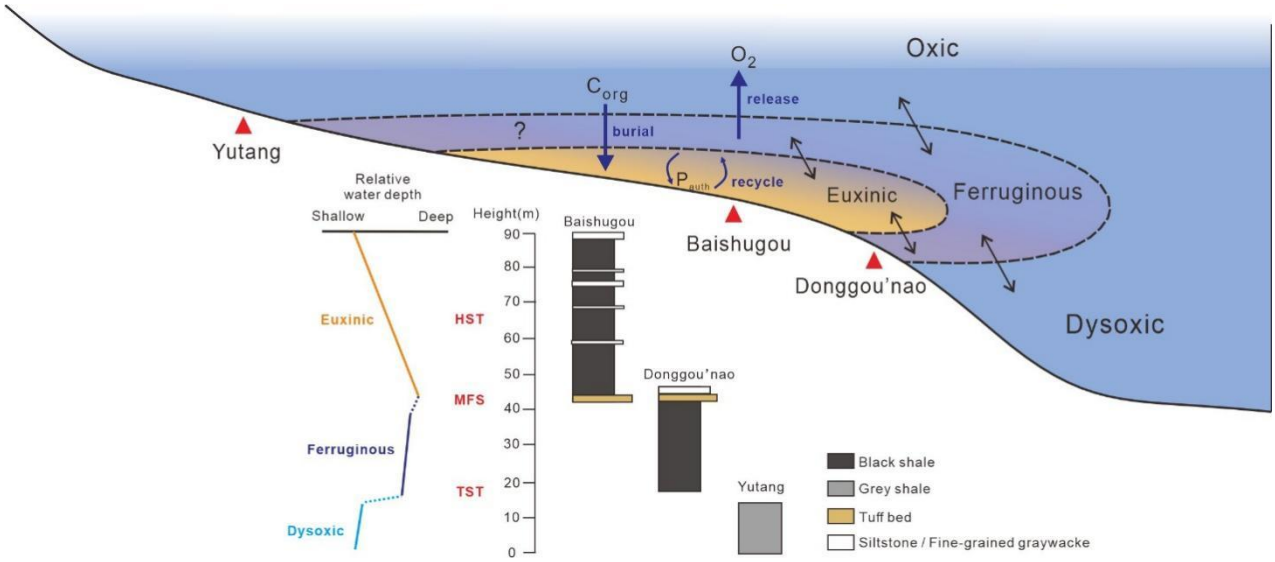

Figure 4. (a)–(d) Secular variability in atmospheric oxygen levels and a compilation of black shale $\delta^{98/95}$Mo values and Mo and P contents of shales through the last 3.5 billion years of Earth history ($\delta^{98/95}$Mo and [Mo] data are from ref. [70]; P data are from ref. [74]; the Xiamaling Formation data are from ref. [89]. The light-blue points with Mo contents <2 ppm are excluded as valid representatives; the Velkerri Formation data are from refs. [14,30,41]).